Journal for ImmunoTherapy of Cancer

Single-cell-based identification of drug synergy with immunotherapy via tumor microenvironment remodeling

Ziruoyu Wang ,[1,2] Junchi Hu ,[1] Kailu Liu,[1] Jie Xu,[1] Jiao Li,[1] Yihang Liu,[1] Qinfeng Ma,[1] Yu Dong,[3] Yunmei Zhu,[1] Kai Zhang,[1] Dexin Wang,[4] Xiaobo Wang,[1] Shuai Wang,[1] Jianbo Pan,[1] Shuai Jiang,[3] Jiaxue Wu,[1] Wei Jiang ,[2] Ling Zhang ,[5] Yongjun Dang [1,5]

To cite: Wang Z, Hu J, Liu K, *et al*. Single-cell-based identification of drug synergy with immunotherapy via tumor microenvironment remodeling. *Journal for ImmunoTherapy of Cancer* 2026;**14**:e014132. doi:10.1136/jitc-2025-014132

► Additional supplemental material is published online only. To view, please visit the journal online (https://doi.org/10.1136/jitc-2025-014132).

Accepted 17 February 2026

For numbered affiliations see end of article.

Correspondence to
Professor Yongjun Dang; yjdang@cqmu.edu.cn

Professor Wei Jiang; jiangw@fudan.edu.cn

Dr Ling Zhang; lingzhang02@hospital.cqmu.edu.cn

ABSTRACT

Background Identifying effective therapeutic drugs in the intricate tumor microenvironment (TME) is challenging, further complicated by the lack of a systematic framework for analyzing TME perturbations in response to therapeutic interventions.

Methods To address this, we established the single-cell RNA sequencing repository of immunomodulatory drugs resource and used the L1000 platform for unbiased screening of 739 immune-modulating compounds across various cancers.

Results Drug responses in mouse model revealed 12 distinct meta-programs associated with TME remodeling, enriched in biological processes such as antigen presentation, tissue repair, and salt stress response. Notably, myeloid-derived suppressor cells were markedly reduced in responsive TMEs compared with other cell types, underscoring their key immunosuppressive role. We developed an MP scoring algorithm to quantify TME responsiveness, which successfully identified allopurinol—a gout medication—as a potent enhancer of anti-programmed cell death protein-1 therapy. This combination led to significant tumor-free outcomes (4/6) in vivo.

Conclusions This work provides a robust framework for assessing TME remodeling that uncovers genes and compounds that significantly modulate immunotherapeutic efficacy.

WHAT IS ALREADY KNOWN ON THIS TOPIC

⇒ Therapeutic responses are strongly influenced by the tumor microenvironment (TME). However, no systematic framework exists to quantify drug-induced TME remodeling across cancers, limiting the rational design of effective immunotherapy combinations.

WHAT THIS STUDY ADDS

⇒ We built the single-cell RNA sequencing repository of immunomodulatory drugs resource and, via unbiased screening of 739 compounds, defined 12 TME meta-programs (MPs) and an MP scoring algorithm that highlight myeloid-derived suppressor cell depletion as a hallmark of response and nominate allopurinol as a potent anti-programmed cell death protein-1 adjunct yielding tumor-free cures in vivo.

HOW THIS STUDY MIGHT AFFECT RESEARCH, PRACTICE OR POLICY

⇒ This framework enables quantitative assessment of TME remodeling to prioritize combination immunotherapies and biomarkers, accelerating preclinical triage and guiding precision immuno-oncology trial design.

BACKGROUND

In the complex and dynamic tumor microenvironment (TME), identifying effective therapeutic drugs remains a significant challenge. This difficulty is further compounded by the lack of a robust framework for systematically analyzing the TME and its interactions with immunotherapy. Cancer biology and therapy have been significantly advanced by our growing understanding of the immunoregulatory mechanisms in TME.[1] Importantly, the functionality of immune cells within the TME is fundamentally influenced by tumor cells themselves. Across many solid tumor types, intratumor heterogeneity (ITH) is a prevalent feature, with neoplastic cells within tumors exhibiting highly variable states characterized by substantial differences in gene expression.[2] ITH drives both tumor resistance and immune evasion. Understanding the "rules" governing diverse phenotypic states could facilitate the development of cellular models predictive of drug synergy.

Recent advances in single-cell transcriptomics and spatial profiling have deepened our understanding of cancer cells and tumor-associated cells, revealing their cellular hierarchies.[3 4] However, a consensus has yet to be reached on which immune cell subtypes are most critical in driving tumor progression, as their importance varies widely across different tumor types, stages, and TME compositions.[5]

Given this complexity, a fundamental strategy to overcome immune evasion may involve reshaping the tumor cells themselves to enhance immune recognition and response. By targeting the intrinsic properties of tumor cells and their interaction with the TME, we may be able to develop more effective therapeutic interventions that can overcome the challenges of immune evasion and resistance to treatment. Recent studies have increasingly focused on targeting tumor cells to improve the efficacy of immunotherapy.[6–8]

Immunotherapies have demonstrated remarkable efficacy against cancers, but durable responses remain elusive for most patients.[9] A major challenge is the insufficient potency of T cells to eradicate large tumor burdens, due to factors such as T-cell exhaustion, senescence, and immunosuppression. In our study, we identified a lower myeloid-derived suppressor cells (MDSCs)-to-immune cell ratio as a hallmark of responsive TMEs, suggesting its utility as a biomarker for predicting drug synergy with immunotherapy. This underscores the need to dissect the immunosuppressive mechanisms—beyond regulatory T cells (Tregs)—that modulate antitumor immunity.[10]

Notably, similar ITH programs have been identified across tumors of the same cancer type, and in some cases even across different cancer types, suggesting that ITH expression programs reflect fundamental aspects of tumor biology.[2] Therefore, we sought to identify consensus hallmarks among related ITH programs from different treatments, which we termed meta-programs (MPs) for identifying drug synergy to augment immunotherapy response. We further extended MP analysis to identify novel immune-regulatory compounds and discovered a drug originally used for gout that demonstrated outstanding antitumor efficacy when combined with anti-programmed cell death protein-1 (PD-1) therapy in vivo. This analysis underscores the potential for developing cellular models to predict drug synergy based on a deeper understanding of the rules governing different phenotypic states.

METHODS

Tumor cell-specific immune infiltration modulatory genes characterization

We systematically identified and characterized tumor cell-specific immune infiltration modulatory genes (TIIMGs) across the eight cancer types, including bladder urothelial carcinoma (BLCA), breast invasive carcinoma (BRCA), colon adenocarcinoma (COAD), head and neck squamous cell carcinoma (HNSC), kidney renal clear cell carcinoma (KIRC), liver hepatocellular carcinoma (LIHC), lung adenocarcinoma (LUAD), and prostate adenocarcinoma (PRAD), with matched cancer cell lines and corresponding drug perturbation profiles in the connectivity map (CMap) database,[11] using a multistep approach. Initially, tumor differential expression genes (TDEGs) were identified via the Wilcoxon rank-sum test on The Cancer Genome Atlas (TCGA) data, with False Discovery Rate (FDR) <0.05 and fold change >2.456 immune-related genes from ImmuCellAI[12] were excluded to minimize bulk RNA sequencing (RNA-seq) bias. Subsequently, immune infiltration (InfiltrationScore) was determined using the ImmuCellAI deconvolution algorithm, and Spearman correlations between expression of TDEGs and InfiltrationScore per sample were calculated, focusing on genes with p<0.05. Finally, TIIMGs were identified by selecting genes upregulated in tumors and negatively correlated with InfiltrationScore (Spearman correlation coefficient <−0.3, p<0.05, unGenes) or downregulated in tumors but positively correlated (Spearman correlation coefficient >0.3, p<0.05, dpGenes). See online supplemental materials and methods for details.

Drug screening based on L1000 platform

The L1000 platform (part of the CMap LINCS resource) details transcriptional responses to small-molecule perturbagens (https://clue.io/data/CMap2020#LINCS2020). (1) Data acquisition: gene expression data for the eight cancer types were sourced from the L1000 database in GCTX file format (level5_beta_trt_cp_n720216×12 328.gctx). The analysis was centered on TIIMGs (dpGenes and unGenes). (2) Data preprocessing: a two-tailed connectivity scores (z-score) threshold of |1.96| (p<0.05) was employed. For dpGenes, z-score ≤1.96 was nullified, eliminating statistically non-significant positive perturbations. Similarly, for unGenes, z-score ≥−1.96 were set to zero to remove non-significant negative perturbations. (3) Scoring and normalization: a perturbation score for both dpGenes (S_{dp}) and unGenes (S_{un}), representing the magnitude of its effect across experimental conditions, was calculated, which was then normalized by subtracting the unGene score (which are negatively selected) from the dpGene score. This difference was divided by the total number of TIIMGs (N_{TIIMG}), defined as the sum of dpGenes and unGenes. The normalized score can be expressed as follows, which quantifies the impact of each perturbation on the selected gene sets in a specific direction.

$$S_{norm} = \frac{S_{dp} - S_{un}}{N_{TIIMG}}$$

(4) Drug identification: drugs with a normalized sum exceeding 1.568, representing at least 80% of TIIMGs significantly affected—were classified as potential targets. Summarized z-scores, derived from the highest quantile, ensured a robust selection of compounds demonstrating substantial modulation of TME. (5) Drug-to-cell recall: to validate the screened drugs, a drug-to-cell assay was performed using 54 compounds across relevant cancer cell lines (figure 1C and online supplemental table S3). Subtle responses were detected with low-dose (≤median, <48 hours) and high-dose (≥median, ≥24 hours) treatments. Significant gene expression changes (max quantile ≥ ±3.891), masking z-scores between −1.645 and 1.645 as NaNs, were analyzed via Spearman's correlation (p<0.05) to identify correlations with immune cell infiltration. An 80% threshold defined significant contributions,

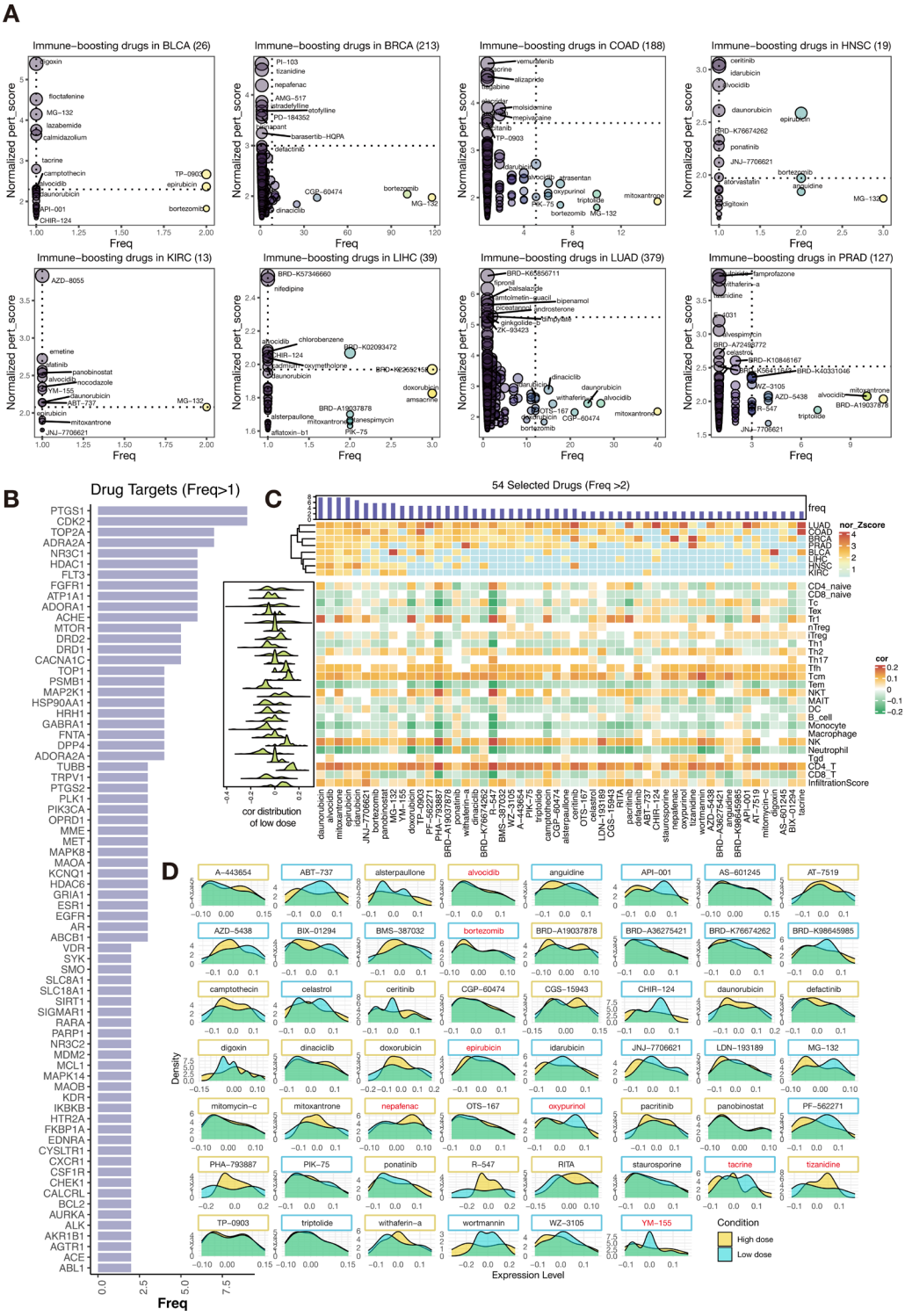

Figure 1 L1000 screening for candidate compounds. (A) Normalized enrichment scores of drugs on TIIMG expression across eight cancer types. Circle size denotes connectivity score; color indicates the frequency ("Freq") of qualifying perturbations per drug. The top 10 candidates lie above the dashed line. (B) Frequency of drug targets among the 739 selected compounds. (C) Heatmap showing Spearman correlations (p<0.05) between DTCGs (low-dose) and immune cell infiltration scores across eight TCGA cancer types (white: non-significant). The left density plot shows correlation distribution per immune cell type. Top heatmap highlights 54 drugs recurrent in ≥3 cancer types, with frequencies noted above. (D) Density distributions of correlation coefficients between DTCGs and immune infiltration for high-dose (yellow) and low-dose (blue) treatments. A colored box above a drug name indicates which dose recruits more immune cells. Drugs selected for in vivo validation are marked in red. BLCA, bladder urothelial carcinoma; BRCA, breast invasive carcinoma; COAD, colon adenocarcinoma; DTCGs, drug-to-cell gene; HNSC, head and neck squamous cell carcinoma; KIRC, kidney renal clear cell carcinoma; LIHC, liver hepatocellular carcinoma; LUAD, lung adenocarcinoma; PRAD, prostate adenocarcinoma; TCGA, The Cancer Genome Atlas; TIIMG, tumor cell-specific immune infiltration modulatory gene.

revealing immunomodulatory effects under both dose conditions (online supplemental figure S3). See online supplemental materials and methods for details.

In vivo drug administration

CT26 murine colon carcinoma cells were enzymatically dissociated and injected into 6–8 weeks old BALB/c mice. Mice were treated subcutaneously with various compounds (alvocidib, bortezomib, epirubicin, vemurafenib, tizanidine, YM-155, oxypurinol, nepafenac, tacrine) at dosages outlined in online supplemental table S4 (intraperitoneal, i.p.; subcutaneous, s.c.; or oral, p.o.) for 2-week cycles, with monitoring of tumor volume and body weight. A separate study used BALB/c or nude mice bearing CT26 tumors, receiving allopurinol (with anti-PD-1 antibody co-treatment) daily or every other day for 17 days. All animals were maintained under specific pathogen-free conditions with controlled temperature, humidity, and a 12-hour light-dark cycle. All procedures adhered to Chongqing Medical University's IACUC guidelines (approval no. IACUC-CQMU-2023-0045). See online supplemental materials and methods for details.

Single-cell RNA-seq analysis

Single-cell RNA sequencing (scRNA-seq) libraries were prepared using two methods: (1) droplet-based 10x Genomics Chromium Single-Cell 3' Kits following the manufacturer's protocol; (2) microwells-based Singleron Matrix system per manufacturer's protocol. Both library types were sequenced on the Illumina NovaSeq 6000 platform and generated unique molecular identifier (UMI) count matrices. The R software (V.3.6.1) and Seurat[13] (V.4.3.0) were used to analyze the scRNA-seq data. Quality control filtered cells based on UMI counts, gene expression, and mitochondrial content. The robust principal component analysis (RPCA) algorithm[14] was used to remove batch effects. Normalized and scaled data were then used for principal component analysis (PCA) and cell clustering. Cell types were annotated based on marker gene expression. Differential expression analysis and Gene Set Enrichment Analysis (GSEA) were performed to identify drug-responsive genes. CellCall (V.1.0.7)[15] was used to analyze cell–cell communication. See online supplemental materials and methods for details.

Identification of NMF (non-negative matrix factorization) programs and meta-programs

Defining robust NMF programs

Each sample was processed individually using the R package NNLM[16] (V.0.4.4). Non-negative matrix factorization (NMF) analysis generated 720 programs across 24 samples, refined to 480 robust programs by excluding low-quality programs. Top 50 genes per program were identified, revealing key gene expression patterns. Overlaps between programs were quantified to identify MPs, defined as shared gene expression motifs among clusters with at least 20 shared genes. Each MP comprised 50 genes and was validated through robust clustering and stability assessments.

Single-sample Gene Set Enrichment Analysis and GSEA analysis of MP enrichment post-treatment

Gene enrichment analysis identified significantly enriched biological process, molecular function, and cellular component Gene Ontology (GO) terms ($p<0.05$) (online supplemental table S6). Single-sample Gene Set Enrichment Analysis (SsGSEA) assessed individual sample MP enrichment, while GSEA compared treatment-induced enrichment to controls using a p value threshold of 0.05. After retaining MP enrichment with significant changes (adjusted p value<0.05) in GSEA, we developed an MP score to quantify MP performance. Given the immune activation potential of Cluster 1 (representing positive immune activation) and Cluster 2 (indicating suppression effects), the MP score ($\boldsymbol{S_{MP}}$), which combines the normalized enrichment scores of Cluster 1 and a weighted reduction of Cluster 2, was calculated as follows:

$$S_{MP} = \sum NES_{Cluster1} - 0.5 \times \sum NES_{Cluster2}$$

See online supplemental materials and methods for details.

Flow cytometric detection of PD-L1 and MHC class I expression in cell lines

MB49 and CT26 cells were treated with allopurinol (AP) at varying concentrations and analyzed using antibody staining. Cells were detached by trypsin digestion and stained with anti-programmed death-ligand 1 (PD-L1) and anti-H2K antibodies, followed by flow cytometric analysis. See online supplemental materials and methods for details.

LC-MS/MS Analysis of inosine in CT26 cell line

CT26 cells treated with AP were analyzed for inosine levels via Shimadzu ultra-high-performance liquid chromatography (UHPLC)-liquid chromatography-tandem mass spectrometry (LC-MS/MS). Supernatants and cell lysates were extracted and dried. Inosine quantification was performed using gradient-elution UHPLC coupled with a triple quadrupole mass spectrometer using multiple reaction monitoring at m/z 269.10. Samples were reconstituted and centrifuged before analysis to ensure accurate measurement of inosine concentrations. See online supplemental materials and methods for details.

B16-OVA and CD8$^+$ T co-culture assays

B16-OVA melanoma cells were pretreated with 50 µM AP or saline for 48 hours. OT-I CD8$^+$ T cells, specific for SIINFEKL, were isolated from the spleens and lymph nodes of OT-I transgenic C57BL/6 mice maintained and stimulated with SIINFEKL in culture medium supplemented with 10% fetal bovine serum (FBS), 1% penicillin-streptomycin, 2 mM L-glutamine, 10 mM HEPES (4-(2-

hydroxyethyl)-1-piperazineethanesulfonic acid), MEM non-essential amino acids, 50 µM β-mercaptoethanol, and 10 ng/mL recombinant human interleukin-2. Activated OT-I $CD8^+$ T cells were then co-cultured with AP-pretreated or saline-pretreated B16-OVA tumor cells at a 2:1 tumor:T-cell ratio for approximately 24 hours. Tumor cell viability post-co-culture was assessed using the CellTiter-Glo Assay. See online supplemental materials and methods for details.

Bulk RNA-seq analysis

Total RNA was prepared and converted to complementary DNA libraries using Illumina's NEBNext kit. Raw FASTQ data was sequenced and cleaned, and then aligned to the GRCm39.112 genome, followed by transcript assembly. Then differential expression analysis and GO enrichment was conducted. See online supplemental materials and methods for details.

Human bladder samples

A retrospective review of electronic medical records identified 50 patients with both bladder cancer and gout at Zhongshan Hospital. Patients were included based on confirmed diagnoses and a history of gout. Clinical data were collected, including anti-PD-1 therapy, concomitant anti-gout medication use, and survival outcomes. The cohort was divided into two groups: 7 patients receiving anti-gout medication during anti-PD-1 therapy, and 43 patients not receiving it. Survival analysis revealed significantly better overall survival (OS) in the group receiving gout medication. Patient metadata was summarized in online supplemental table S8.

Statistics

All statistical analyses were conducted using GraphPad Prism V.10, R (V.3.6), and Python (V.3.8.3). Statistical significance was determined through unpaired two-tailed Student's t-test, one-way analysis of variance (ANOVA) with Dunnett's post hoc test, or two-way ANOVA with Dunnett's post hoc test. Significance levels are indicated by asterisks as follows: *p<0.05, **p<0.01, ***p<0.001. Data are presented as mean±SD for all columns, while mouse tumor volume data are shown as mean±SEM. In one-way or two-way ANOVA with post hoc tests, asterisks are shown only for the specific comparisons of interest.

RESULTS

Tumor cell-specific immune infiltration modulatory genes identification

This study deployed the ImmuCellAI[12] tool to deconvolute TCGA data, investigating the relationship between immune cell infiltration scores[17] and TDEGs across eight cancer types (BLCA, BRCA, COAD, HNSC, KIRC, LIHC, LUAD, and PRAD), with matched cancer cell lines also applicable to the L1000 platform (figure 2A). This approach identified TIIMGs, classifying them into two categories: "dpGenes" (downregulated in tumors yet positively correlated with infiltration) and "unGenes" (upregulated in tumors but negatively correlated) (Methods). Then, by employing the L1000 platform[11 18] alongside flow cytometry and scRNA-seq in a murine model, the study delved into the immune cell infiltration dynamics and tumor cellular responses to diverse therapeutic interventions, thereby enriching the comprehension of the tumor-immune interface (figure 2A).

The analysis began with TCGA DEGs, excluding 456 immune-related genes to define TDEGs (online supplemental table S1, Methods). Correlation analysis between deconvoluted immune cell data and overall infiltration scores (online supplemental table S1) revealed a strong positive correlation with macrophages, cytotoxic T cells, and dendritic cells, but a negative correlation with neutrophils in pan-cancer (figure 2B, online supplemental figure S1), validating the infiltration score as a key metric. Linking infiltration scores to TDEG expression categorized TIIMGs into dpGenes and unGenes (online supplemental figure S2), revealing significant heterogeneity across cancers. COAD possessed the largest TIIMG set (792 dpGenes and 83 unGenes), while KIRC had the smallest, highlighting diverse TME and immune evasion strategies (online supplemental figure S2, online supplemental table S2). We further cataloged key modulatory genes: upregulated chemokines and inflammatory mediators like PTGDS,[19] PRELP,[20] and FCN1 were implicated in TME remodeling (figure 2C), whereas downregulated genes such as TARBP1,[21] KAT2A, and ITGA6, SLC38A1, and CDK3 suggested diminished tumor-promoting functions (figure 2D). These cancer-specific TIIMG patterns uncover distinct immune regulatory networks, offering novel targets for immunotherapy.

L1000 screening for immunomodulatory drugs

The significant variation in TIIMGs across the eight cancer types underscores the need for cancer-specific drug development. Using the L1000 platform, we pinpointed unique drug candidates for each cancer type by targeting individual TIIMGs in matched cell lines (figure 1A, Methods). Higher perturbation scores indicated stronger modulation of TIIMG expression, correlating with desired therapeutic effects. A total of 739 compounds were identified, with 80.1% being specific to a single cancer type (online supplemental figure S3A, online supplemental table S3), highlighting their target heterogeneity (figure 1B). Many Food and Drug Administration-approved drugs, such as panobinostat, ceritinib, ponatinib, epirubicin, and crizotinib, were shown to be promising for cancer therapy. Recent validations have extended to drugs acting on ADRA2A[22] and PTGS1[23] to stimulate immune response, contributing to the evolving landscape of cancer therapeutics. Notably, non-cancer drugs like tizanidine (spasticity), oxypurinol (heart failure, gout), nepafenac (cataract prevention), and tacrine (Alzheimer's) show promise for cancer

treatment, highlighting their versatility and broad therapeutic potential.

Our focused analysis on 54 drugs, which have demonstrated relevance across more than two cancer types (figure 1C), revealed compounds targeting topoisomerases (eg, epirubicin, doxorubicin, camptothecin, mitomycin-c); cyclin-dependent kinases (CDKs) (eg, alvocidib, dinaciclib, PF-562271, CGP-60474); histone deacetylase 1 (HDAC1) (eg, panobinostat, vorinostat); and additional targets such as withaferin A (NF-κB), ceritinib (ALK), digoxin (potassium channel) and wortmannin (PI3K) (online supplemental table S3). Our screening methodology yielded a diverse array of compounds, demonstrating robustness and clinical relevance by targeting essential pathways across a range of diseases, especially tumors (figure 1C, online supplemental table S3).

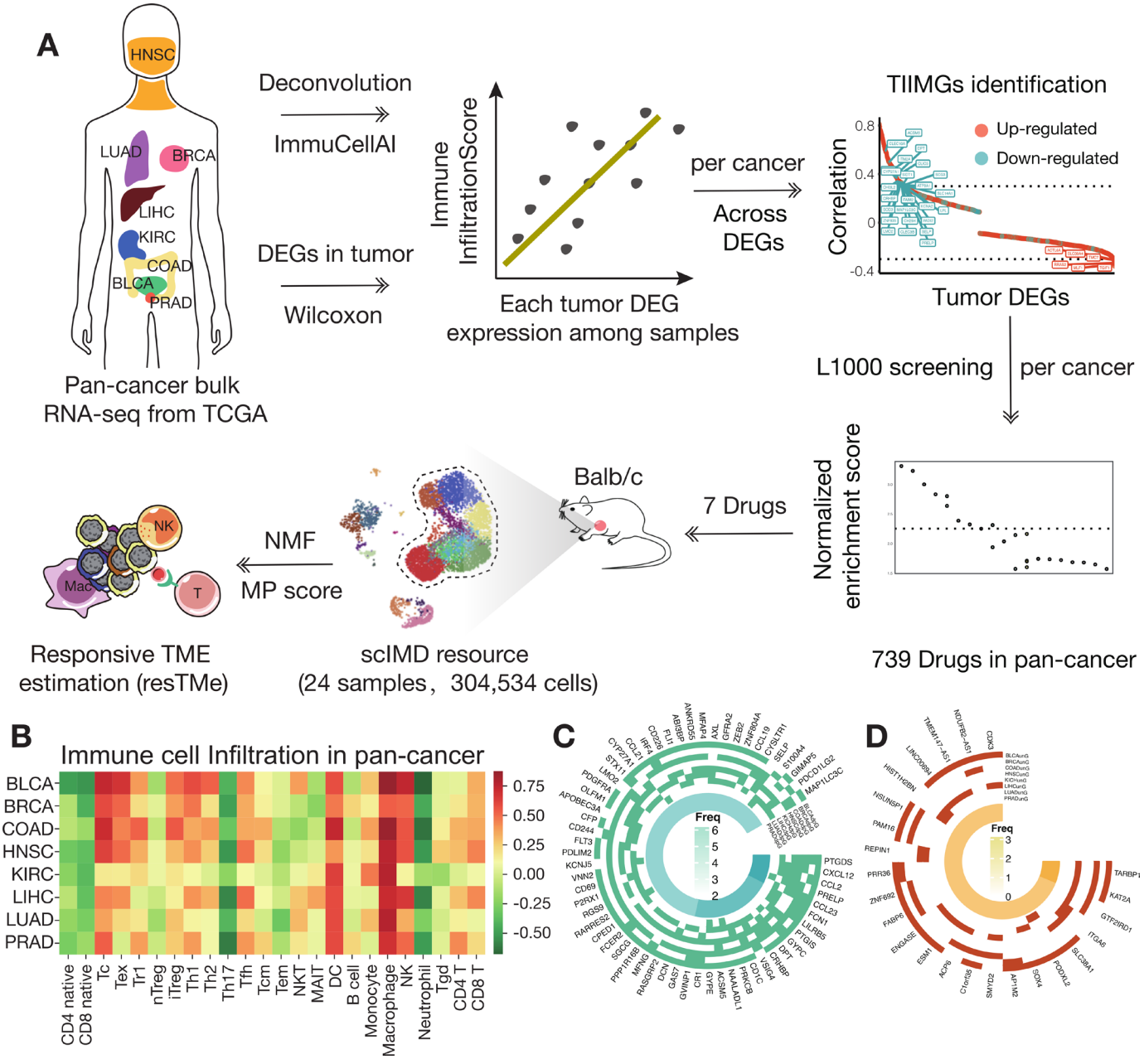

Figure 2 TIIMGs identification from pan-cancer bulk RNA-seq. (A) Workflow of construction of scIMD resource. (B) Pan-cancer Spearman correlation (p<0.05) between infiltrationScore and individual immune cell types estimated by ImmuCellAI. (C–D) Identification of TIIMGs in eight different cancer types, with dpGenes shown in blue (C) and unGenes in red (D). BLCA, bladder urothelial carcinoma; BRCA, breast invasive carcinoma; COAD, colon adenocarcinoma; DEG, differential expression gene; HNSC, head and neck squamous cell carcinoma; KIRC, kidney renal clear cell carcinoma; LIHC, liver hepatocellular carcinoma; LUAD, lung adenocarcinoma; MP, meta-program; NK, natural killer; NMF, non-negative matrix factorization; PRAD, prostate adenocarcinoma; RNA-seq, RNA sequencing; scIMD, single-cell RNA sequencing repository of immunomodulatory drug; TCGA, The Cancer Genome Atlas; TIIMG, tumor cell-specific immune infiltration modulatory gene; TME, tumor microenvironment.

To validate the efficacy of the identified drugs, we performed a drug-to-cell recall (Methods) using the L1000 platform to identify perturbed genes and associated immune cell changes via the immuCellAI algorithm. Over 80% of the drugs were linked to increased infiltration scores, validating the reliability of our screening (figure 1C). Notably, immunomodulatory effects were not strictly dose-dependent. The high-dose treatment resulted in fewer perturbation IDs but more perturbed genes (online supplemental figure S3B), likely due to cytotoxic effects. In contrast, the low-dose treatment produced more perturbation IDs with slightly fewer perturbed genes (online supplemental figure S3C), suggesting non-cytotoxic effects. Indeed, we observed distinct impacts on immune cell infiltration in both low and high dose groups (figure 2D, S3D), with a general change in cells such as CD4 naive, Tex, Tr1, and CD8 T cells. Importantly, 50% of the drugs at low concentrations enhanced immune cell infiltration, aligning with recent evidence that low-dose therapies can synergize with immunotherapy.[24–28] We further prioritized 54 multicancer drugs acting on key pathways such as CDKs, HDAC1 and PI3K and validated the efficacy of identified drugs, with low-dose treatments showing non-cytotoxic immunomodulatory effects. This systematic approach highlights promising candidates for combination immunotherapy strategies.

Candidate drugs exhibit various immunomodulatory effects in vivo

To evaluate the immunomodulatory potential of candidate compounds, we selected eight drugs from the top 54 candidates (figure 1C). Three drugs (alvocidib, nepafenac, tizanidine) exhibited immune-enhancing tendencies at high doses, while the remaining five (bortezomib, epirubicin, oxypurinol, tacrine, YM-155) functioned as low-dose immune boosters (figure 1D). These drugs target diverse pathways including CDKs, proteasome, DNA topoisomerase II, B-raf, α2-adrenergic receptor, BIRC5, Survivin, xanthine oxidase, COX1 (PTGS1), COX2 (PTGS2), HNMT, AChR, and ChE (online supplemental table S3). Additionally, we selected vemurafenib, a drug uniquely identified in the COAD. These selections included agents with known antitumor efficacy as well as drugs primarily indicated for non-oncological conditions.

Using a syngeneic CT26 tumor model in BALB/c mice, we evaluated candidate compounds at both high and low doses (figure 3A, online supplemental table S4, Methods). High dosage regimens, based on prior tumor suppression benchmarks (online supplemental table S4), often proved effective but frequently suppressed TME immune cell infiltration, likely due to cytotoxicity (figure 3B). Conversely, low-dose regimens minimized potential toxicity while eliciting immunological responses (figure 3B). For instance, high-dose epirubicin effectively controlled tumor growth but reduced immune cell presence (figure 3C), illustrating how conventional chemotherapy may compromise antitumor immunity. These results suggest that low-dose regimens offer a favorable approach for TME remodeling, preserving immune function.

Varied immunomodulatory effects across drugs at the scRNA-seq level

To evaluate drug-induced changes in the tumor immune microenvironment, we performed scRNA-seq on CT26 tumors from seven treatment groups administered with low dose alvocidib, bortezomib, epirubicin, vemurafenib, nepafenac, YM-155, and oxypurinol, establishing the scRNA-seq repository of immunomodulatory drugs dataset. To ensure the reliability and reproducibility of our data, each treatment condition was conducted using three biological replicates (online supplemental figure S4A). This comprehensive dataset encompassing 304,543 cells, which included 236,626 cancer cells, 64,651 immune cells, 2,502 cancer-associated fibroblasts (CAFs), and 764 endothelial cells (online supplemental figure S4B). In concordance with our hypothesis, drug treatments generally reduced cancer cell proportions while increasing immune cell infiltration (online supplemental figure S4B).

We identified 11 distinct cellular clusters within TME (figure 4A, online supplemental figure S4C) and analyzed differential gene expression, pathway enrichment (online supplemental figure S5), and cell–cell communication networks (online supplemental figure S6) across treatment conditions. The results indicated significant variability in the immunomodulatory effects of the different drugs (figure 4B, online supplemental figure S5, S6). Notably, oxypurinol significantly altered macrophages and dendritic cells (DCs) populations while reducing CAFs and MDSCs (figure 4B). The downregulation of Arg1 in macrophages may suggest a shift towards a pro-inflammatory phenotype (online supplemental figure S5E, S6). Concurrent immune activation in cancer cells indicated oxypurinol's dual role in direct tumor suppression and immune modulation (online supplemental figure S5E).

Despite variations in immune cell infiltration patterns across treatments, we consistently observed enhanced recruitment of T cells, NK cells, NKT cells, and DCs, alongside reduced cancer cell prevalence. Notably, oxypurinol, epirubicin, vemurafenib, nepafenac, and YM-155 significantly increased the macrophage infiltration by 147.3%–220.3%, while reducing MDSC infiltration by 57.1%–14.3% versus dimethyl sulfoxide (DMSO) control (figure 4B). Growing evidence indicated that MDSCs also play a role in developing resistance to cancer treatments, especially immunotherapies.[10]

Our analysis delved into various T-cell subsets, including memory T cells, γδ T cells, Treg, naïve T cells (T_naive), and exhausted T effector cells (figure 4C). We discovered that alvocidib and bortezomib promoted T_naive expansion, whereas epirubicin, oxypurinol, and vemurafenib treatments expanded exhausted T cells while reducing Tregs (figure 4D,E). These findings suggest a potential limitation of low-dose monotherapy with these

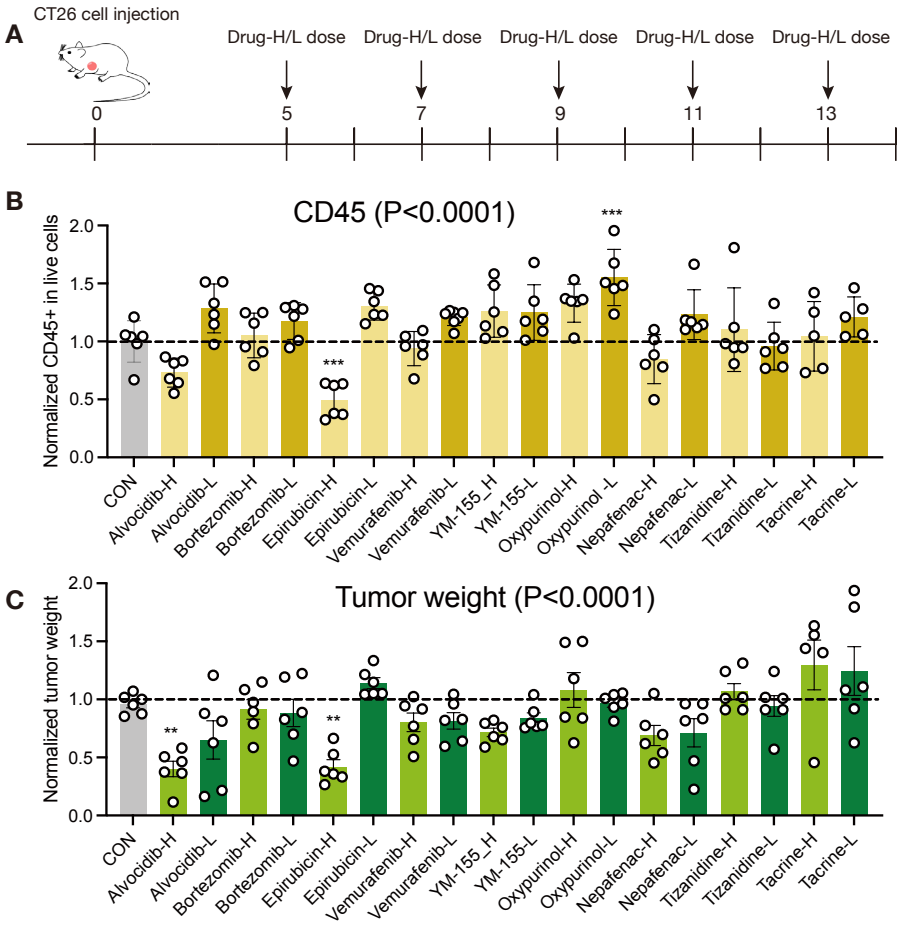

Figure 3 Evaluation of drug immunomodulatory effects in vivo. (A) Administration model for all selected drugs in a mouse model. Each drug was administered at high and low doses. (B) Relative CD45⁺ fluorescence intensity in tumors at endpoint, normalized to the batch-matched control group (n=6 mice/group; mean±SD; p values from one-way ANOVA with Dunnett's multiple comparison test). (C) Relative tumor weight at endpoint, normalized to the batch-matched control (n=6 mice/group; mean±SEM; p values from one-way ANOVA with Dunnett's multiple comparison test). ANOVA, analysis of variance.

drugs in halting tumor progression due to the increase in exhausted T-cell populations. However, these findings suggest that combining these drugs with anti-PD-1 antibodies could enhance antitumor immunity.

Above all, we conducted a further evaluation of the identified drugs on TME remodeling, focusing on cell infiltration, DEG, GSEA, and cell interaction levels based on scRNA-seq data. Our findings suggested that oxypurinol, epirubicin, and vemurafenib endowed these cells with an immune-responsive phenotype and were more susceptible to immune checkpoint blockade (ICB).

Identifying consensus meta-programs of tumor cells

ITH poses a significant challenge to cancer therapy by driving drug resistance and reshaping TME. The observation that tumor cells clustered into nine distinct clusters at a resolution of 0.6 suggests substantial post-treatment ITH (online supplemental figure S4A). To comprehensively characterize ITH, we applied de novo NMF[2 29] to cancer cells, identifying recurrent expression programs across the 24 samples (figure 5A, online supplemental table S6, Methods). After rigorous quality control, we retained 480 robust NMF programs that captured key biological variations without technical biases. These programs were consolidated into 12 consensus MPs, each comprising 50 coordinately expressed genes (figure 5, online supplemental tables S6, S7). Functional annotation revealed that these MPs encompassed diverse biological processes, including antigen processing and presentation, cell division, cellular response to salt stress, post-transcriptional modifications, DNA replication, interferon response, glycolysis and pyruvate metabolism, amide metabolism, RNA metabolism, tissue regeneration, translation processes, and antigen presenting cell differentiation (figure 5B).

Notably, MPs 1/3/6/8/10/12 were predominantly enriched in antigen processing and presentation pathways. This enrichment highlights the essential role of major histocompatibility complex (MHC) class I-mediated antigen presentation in the activation of cytotoxic T cells and subsequent tumor elimination. The strong association of these MPs with antigen processing pathways suggests that successful immunotherapy requires not only

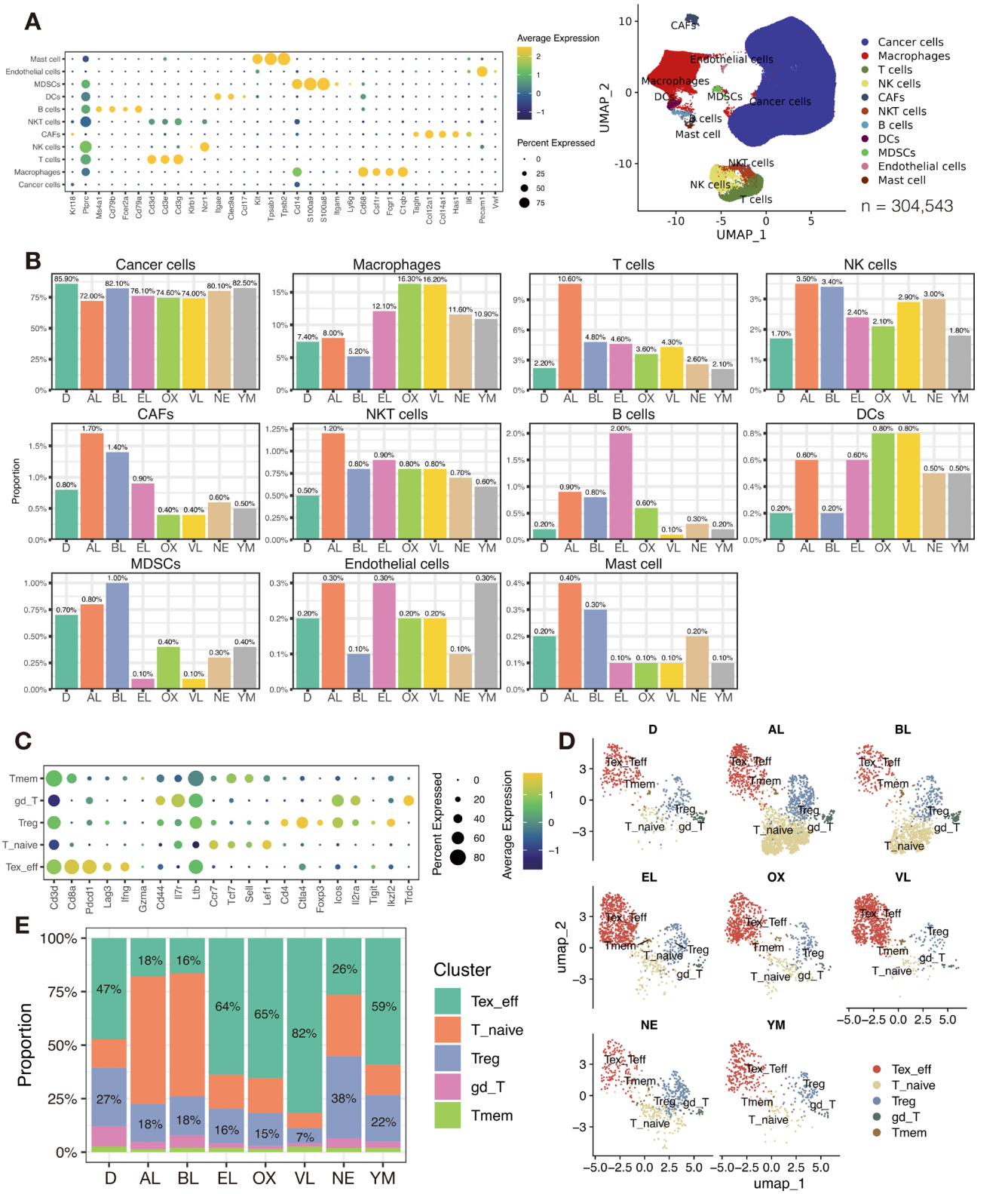

Figure 4 scRNA-seq analysis of various drug perturbations. (A) UMAP visualization and bubble heatmap showing marker gene expression across 11 major cell clusters identified from CT26 tumors (n=24 samples; three replicates each for DMSO and seven drugs). (B) Changes in the proportions of each cell cluster in drug-treated versus DMSO-treated tumors. (C) Expression levels of key T-cell markers are shown in a bubble heatmap for five distinct T-cell subsets: Tmem, gd_T, Treg, T_naive, and Tex_eff T cells. (D) Spatial representation of five T-cell types under each treatment condition. (E) The proportions of T-cell subsets following drug exposure. AL, alvocidib; BL, bortezomib; CAFs, cancer-associated fibroblasts; D, DMSO (dimethyl sulfoxide); DC, dendritic cell; EL, epirubicin; gd_T, γδ; MDSC, myeloid-derived suppressor cell; NE, nepafenac; NK, natural killer; NKT, NK T cell; OX, oxypurinol; scRNA-seq, single-cell RNA sequencing; Tex_eff, exhausted effector; Tmem, memory T cells; T_naive, naïve T cells; Treg, regulatory T cell; UMAP, uniform manifold approximation and projection; VL, vemurafenib; YM, YM-155.

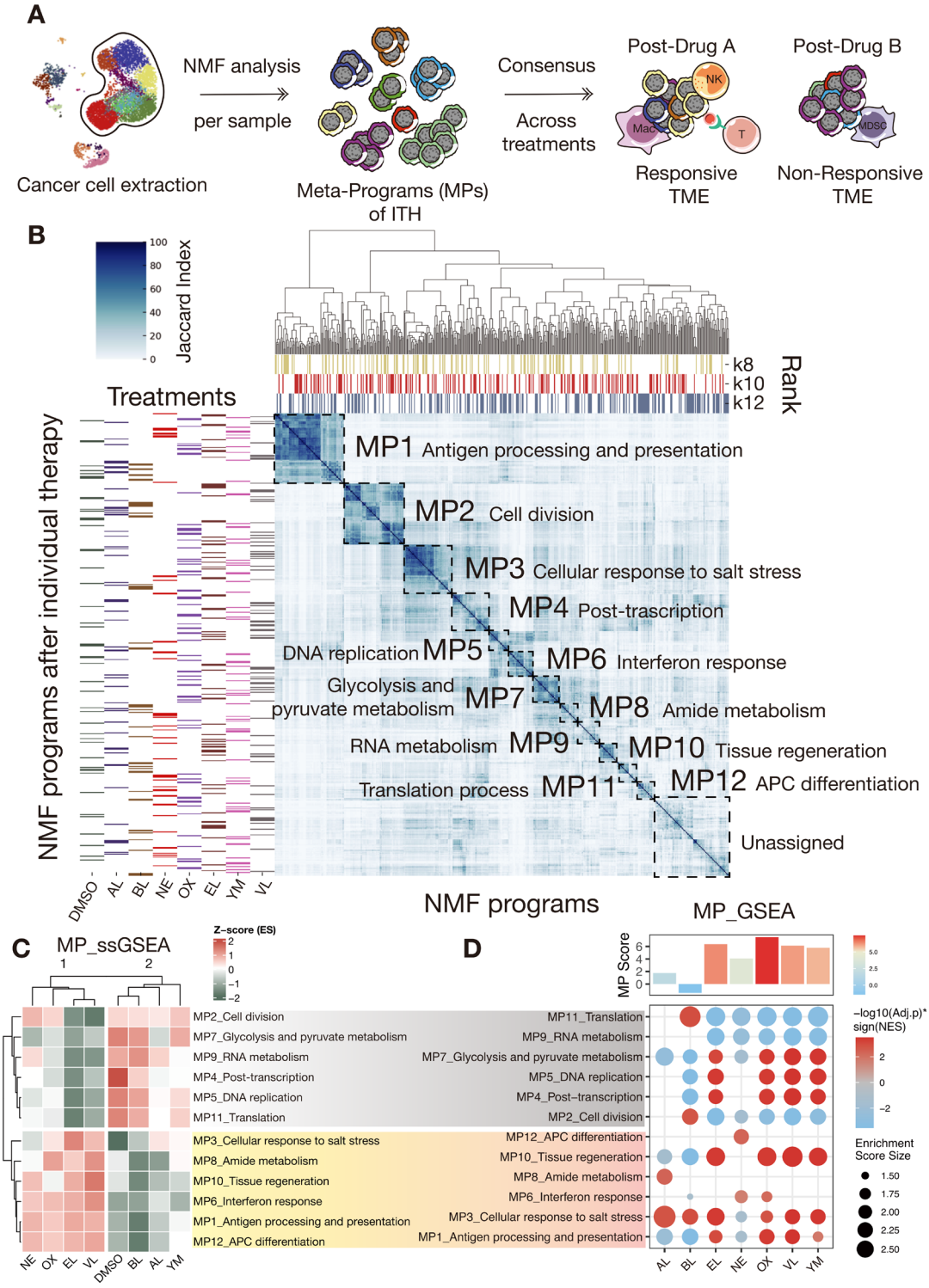

Figure 5 Characterization of MPs and their functional annotations. (A) Schematic outlining the derivation of MPs from an annotated collection of scRNA-seq datasets. (B) Heatmap of Jaccard similarity indices for comparisons among 480 robust NMF programs (based on their top 50 genes), ordered by hierarchical clustering. Programs are grouped into distinct MP families (numbered and separated by dashed lines). NMF was performed with multiple factorization ranks (K=8, 10, 12). (C) ssGSEA ES of MPs in samples treated with DMSO and seven drugs, showing treatment-induced variations in MP activity. (D) Top: bar plot of MP scores. Bottom: GSEA bubble plot displaying pathways in cancer cells that are significantly altered (adjusted p<0.05) in each treatment group versus DMSO. Bubble color reflects $-\log_{10}$ (adjusted p value) × sign (NES), with red and blue indicating upregulation and downregulation, respectively. Bubble size corresponds to the NES. AL, alvocidib; APC, antigen presenting cell; BL, bortezomib; D, DMSO (dimethyl sulfoxide); EL, epirubicin; ES, enrichment score; GSEA, Gene Set Enrichment Analysis; ITH, intratumor heterogeneity; MP, meta-programs; NE, nepafenac; NES, normalized enrichment score; NK, natural killer; NMF, non-negative matrix factorization; OX, oxypurinol; ssGSEA, single-sample Gene Set Enrichment Analysis; scRNA-seq, single-cell RNA sequencing; TME, tumor microenvironment; VL, vemurafenib; YM, YM-155.

enhanced immune cell infiltration but also functional antigen presentation capabilities within the TME (online supplemental figure S7). These MPs provide a framework for understanding treatment-induced TME remodeling mechanisms.

MP score for novel immunoregulatory drug discovery

To characterize post-treatment ITH, we implemented ssGSEA[30] across the 12 MPs, revealing a clear bifurcation into two distinct clusters (figure 5C). Notably, Cluster 2, comprising MPs 3, 8, 10, 6, 1, and 12, exhibited significant enrichment following administration of nepafenac, epirubicin, oxypurinol, and vemurafenib, while the other treatments resembled DMSO controls. Most MPs in Cluster 2, despite functional diversity, shared association with the antigen processing and presentation pathway (online supplemental figure S7), highlighting the pivotal role of MHC class I-mediated antigen presentation in antitumor immunity. Additionally, our findings propose a potential influence of cellular response to salt stress in shaping tumor immunity, as recent studies have shown that sodium chloride in the TME boosts T-cell metabolic fitness and cytotoxicity.[31 32] Therefore, we hypothesize that the drugs enriching MPs in Cluster 2 may coordinate a more significant impact on TME remodeling than those in Cluster 1.

To compare post-treatment differences, we performed GSEA on DEGs identified after drug treatments (online supplemental table S5) and evaluated MP performance across these treatments (figure 5D). We developed an MP scoring system to quantify treatment effects (Methods) based on MP enrichment with significant changes (adjusted p value<0.05) and revealed that oxypurinol was the top-performing compound (figure 5D). This aligns with L1000 (figure 1D) and scRNA-seq analyses (figure 4B, online supplemental figure S5,6), suggesting its strong TME-remodeling capacity. Additionally, vemurafenib[33] and epirubicin[34] also demonstrated favorable scores, consistent with reported immunotherapy synergism. Given limited documentation of oxypurinol's antitumor effects, we further investigated its combination with PD-1 blockade.

Crucially, our pipeline based on the MP score provides a valuable tool for discovering novel immunoregulatory drugs. By analyzing DEGs from bulk RNA-seq data via GSEA, it enables efficient identification of potential drug candidates. We have developed a user-friendly web application, resTMe (http://www.danglab.ac/), and R package resTMe (https://github.com/DangLab-CQMU/resTMe), for broader application in drug discovery.

Allopurinol treatment strongly enhanced immunotherapy

Based on oxypurinol's high MP score and limited understanding of its antitumor role, we investigated AP—its prodrug with superior bioavailability—for TME modulation. We hypothesized AP could enhance anti-PD-1 therapy efficacy.[35–37] Based on gout-related dosing regimens,[36] we treated CT26 tumor-bearing BALB/c mice with high (100 mg/kg) or low (20 mg/kg) doses of AP every other day, combined with anti-PD-L1 therapy starting 5 days post-tumor inoculation. We observed that high-dose AP exerted minimal effects on tumor regression. In contrast, low-dose AP exhibited a trend toward 35.1% tumor control, and when combined with PD-L1 treatment, it resulted in a significant 44.6% tumor regression, without significant systemic toxicity (online supplemental figure S8A–E). The absence of tumor control in nude mice confirmed the immune-dependent mechanism of AP's action (online supplemental figure S8F-I).

Given that AP is metabolized into its active form, oxypurinol, with an in vivo half-life of 14–30 hours, and considering that gout patients typically receive a daily dose of 200–300 mg[35], we optimized a daily oral regimen of AP at 10 mg/kg, in combination with anti-PD-1 therapy two times a week (figure 6A). We observed remarkable efficacy: AP pretreatment alone reduced tumor weight by 77.5% (figure 6D), while combination therapy achieved complete tumor eradication in 4/6 mice (figure 6E), with minimal toxicity (figure 6A–H). Enhanced CD8+T cell infiltration in tumor-draining lymph nodes suggested improved T-cell recruitment (online supplemental figure S8J). Tumor-draining lymph node (TdLN)-derived tumor-specific memory cells exhibited superior antitumor therapeutic efficacy and were characterized as bona fide responders to PD-1/PD-L1 blockade.[38]

Mechanistic investigations revealed AP significantly upregulated both PD-L1 (figure 6I) and MHC class I levels (figure 6J), indicating enhanced tumor immunogenicity. Similar results were confirmed in the bladder cell line MB49 (online supplemental figure S8K,L). To further investigate the mechanism underlying AP's effects, previous studies indicated that inosine enhances tumor immunogenicity[39] and $CD8^+$ T cell[40] or chimeric antigen receptor (CAR)-T cell[41] function, improving sensitivity to ICB.[42] Since AP could increase inosine levels via the salvage pathway, we hypothesize that this may contribute to its immunomodulatory effects (figure 6N). Using mass spectrometry, we measured inosine levels in both culture supernatants and cell lysates. Remarkably, inosine levels in supernatants increased by ~500-fold fold after treatment with 25 µM AP and up to 1000-fold after 50 µM AP treatment (figure 6K), whereas no significant changes were detected in cell lysates (figure 6L), suggesting active export of inosine extracellularly. To further validate AP's effect on T-cell activation, we used a classical B16-OVA and OT-I $CD8^+$ T cell co-culture model. Treatment with 50 µM AP significantly enhanced T-cell-mediated cytotoxicity, reflected by a twofold increase in OT-I T-cell effector activity and therapeutic reinvigoration (figure 6M). Collectively, AP treatment enhances inosine synthesis via the salvage pathway, leading to increased tumor cell inosine export that supports T-cell function within the TME. In parallel, inosine upregulates MHC class I and PD-L1 expression, boosting tumor immunogenicity and checkpoint engagement (figure 6N). Consequently, AP

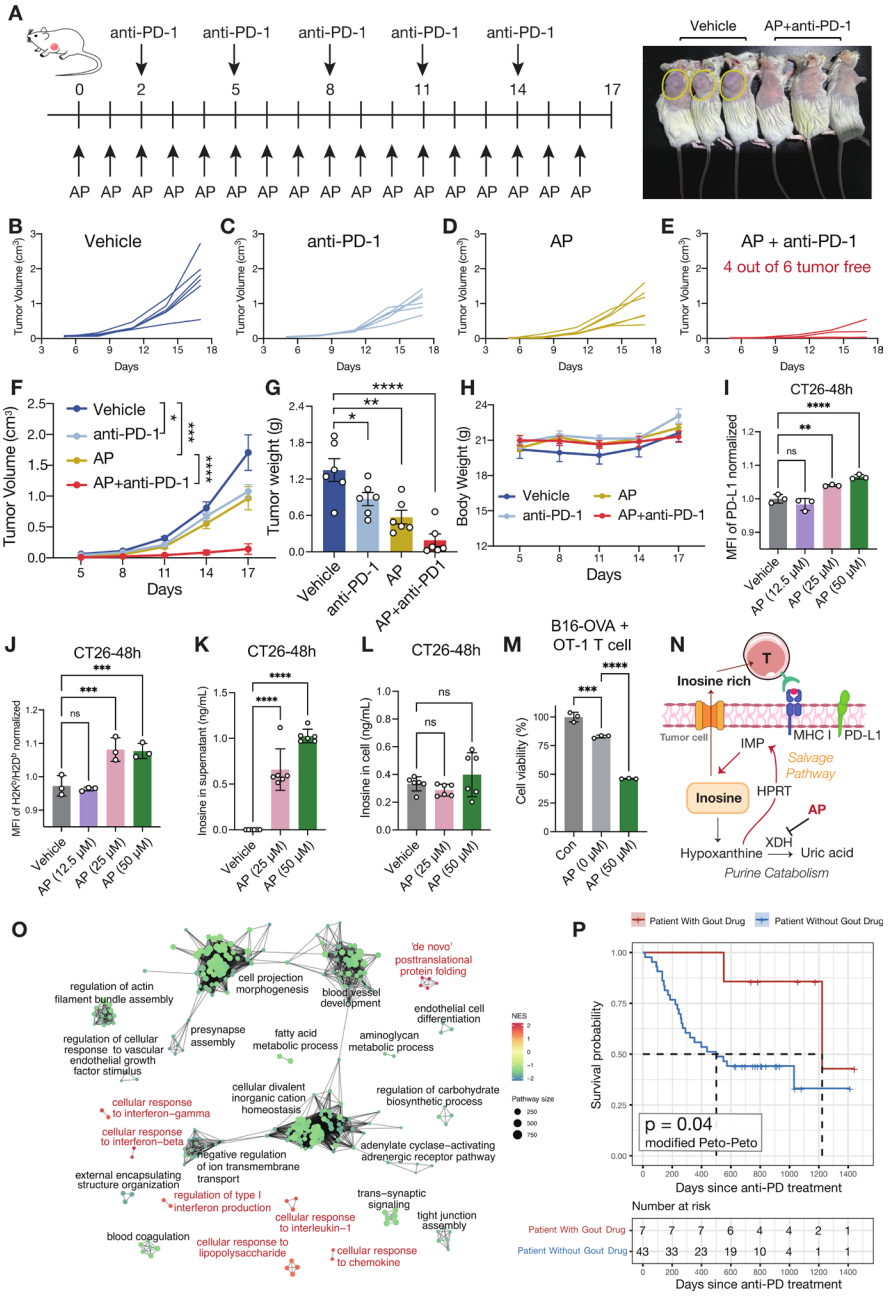

Figure 6 Synergistic tumor suppression by AP combined with anti-PD-1 in vivo. (A) Treatment schedule (AP: 10 mg/kg, oral, daily; anti-PD-1: 10 mg/kg, i.p., two times a week) and representative images. (B–E) Individual tumor growth curves in CT26-bearing BALB/c mice treated with vehicle, anti-PD-1 alone, AP alone, or anti-PD-1 + AP. (F, G) Summary of tumor volume (F) and endpoint tumor weight (G) across treatment groups (mean±SEM). (H) Body weight measurements during treatment. (I–J) Flow cytometry analysis showing increased expression of PD-L1 (I) and MHC class I (H2-Kb/H2-Db) (J) on CT26 cells after 48 hours treatment with AP (12.5, 25, and 50 µM). (K–I) LC-MS/MS quantification of inosine in CT26 cell culture supernatants (K) and cell lysates (L) following 48 hours AP treatment. (M) Relative viability of B16-OVA tumor cells in co-culture with OT-1 T cells. OT-1 T cells were pretreated with 50 µM AP or vehicle for 48 hours, then co-cultured with B16-OVA cells at an effector-to-target ratio of 2:1 for 24 hours. The control (Con) group included B16-OVA cells cultured without OT-1 T cells. (N) Schematic illustration of AP-mediated metabolic reprogramming. XDH inhibition elevates hypoxanthine and inosine via the salvage pathway, potentially enhancing immunogenicity and T-cell function. (O) GSEA of bulk RNA-seq from AP-treated tumors highlighting enriched immune-related pathways (red). (P) Survival analysis of bladder cancer patients on anti-PD-1 therapy with and without gout medications (AP, febuxostat). Data are presented as mean±SEM (tumor/body weight) or mean±SD (flow, LC-MS/MS, viability). P values calculated by two-way ANOVA and Dunnett's multiple comparison analysis. *, **, ***, **** and ns denote p<0.05, 0.01, 0.001, 0.0001, and not significant, respectively. ANOVA, analysis of variance; AP, allopurinol; GSEA, Gene Set Enrichment Analysis; HPRT, hypoxanthine phosphoribosyltransferase; IMP, inosine 5'-monophosphate; i.p., intraperitoneal; LC-MS/MS, liquid chromatography-tandem mass spectrometry; MFI, mean fluorescence intensity; MHC, major histocompatibility complex; PD-1, programmed cell death protein-1; PD-L1, programmed death-ligand 1; RNA-seq, RNA sequencing; XDH, xanthine dehydrogenase.

shows strong synergistic efficacy with anti-PD-1 therapy in vivo.

Bulk RNA-seq of tumors from AP-treated mice showed enriched immune activation pathways and suppressed proliferation signatures (figure 6O, online supplemental table S7). Consistent with our MP framework, AP-treated samples significantly enriched Cluster 2 MPs, achieving a positive MP score of 6.12 (online supplemental figure S8M).

Further supporting these findings, an observational study of 50 patients with bladder cancer undergoing anti-PD-1 therapy for gout treatment with medications like AP or febuxostat showed that those receiving gout medication had significantly better OS compared with those who did not receive such treatments (figure 6P, online supplemental table S8, Methods). This clinical evidence underscores the immunomodulatory effects of AP and its synergistic interaction with anti-PD-1 therapy.

Taken together, our results demonstrate that AP enhances tumor immunogenicity and T-cell function by promoting inosine production and export, thereby reshaping the TME. These effects lead to enhanced efficacy of anti-PD-1 therapy, presenting a promising strategy to improve the therapeutic outcomes of ICB.

DISCUSSION

Identifying effective therapeutic drugs in the complex TME is challenging, exacerbated by the lack of a systematic framework for analyzing TME interactions with therapies. Our study addresses this by introducing a framework using multidrug scRNA-seq to characterize responsive TMEs. This approach improves understanding of the TME and provides insights into immunotherapy development and drug synergies. By analyzing the transcriptome as a proxy for a cancer cell's "global" state, we reveal profound cellular heterogeneity. Our study focuses on intratumoral heterogeneity, offering a deeper understanding of the drug factors shaping cellular states within the TME.

To identify TIIMGs, we used a comprehensive immune cell infiltration index instead of focusing on specific immune cell types, given the highly heterogeneous and multifaceted roles immune cells play within tumors. Many immune cells possess multifaceted and sometimes obscure functions.[3] For example, tumor-associated macrophages (TAMs) display a spectrum of states beyond the traditional M1/M2 classification.[43–45] Drug-induced TME remodeling typically affects only certain immune cell types, leading to subtle changes at the aggregate level.

We demonstrated a strong correlation between the MP score and MDSC infiltration among drugs. MDSCs, highly immunosuppressive cells in TME, play a crucial role in limiting T cell-mediated antitumor immunity and promoting resistance to cancer treatments.[10] Targeting MDSCs by recruitment inhibition or neutralizing their suppressive effects presents a promising strategy to enhance cancer therapy efficacy.

Notably, we found that AP is a potent synergistic agent when combined with anti-PD-1 therapy, particularly in a pretreatment model. AP's inhibition of XO led to an increase in hypoxanthine, which was subsequently converted to inosine 5'-monophosphate and inosine via the purine salvage pathway.[46] Evidence suggested that inosine enhanced the bioenergetic activity of T effector cells, thereby boosting the efficacy of anti-PD-1 therapy.[40] We confirmed that AP activated and recruited Teff cells through the elevation of inosine, contributing to its synergistic effect with anti-PD-1 treatment. Notably, the human equivalent dose of 10 mg/kg daily for mouse low-dose AP treatment corresponded to approximately 0.81 mg/kg daily, significantly lower than the standard gout maintenance dose (200–300 mg daily). This low dose was expected to have minimal side effects in individuals with normal renal function.[35 36] These findings suggest that low-dose AP could potentially be used as a preventive measure against tumor development, though further clinical trials will be needed to confirm this potential.

The main limitation of this study is that the drug scRNA-seq data were derived from mouse models. Incorporating more data from human-derived models, such as patient-derived organoids or patient-derived xenografts, would enhance the robustness and clinical relevance of the predictive model.

In conclusion, we developed a multidrug atlas to map transcriptional ITH in detail. To support its application in future research, we provide the resTMe website and R package, enabling the quantification and visualization of the MPs identified in this study using new post-treatment bulk RNA-seq datasets in cell models. This framework can be refined through further research and will enhance our understanding of ITH, contributing to innovative therapeutic strategies.

Author affiliations
[1]Basic Medicine Research and Innovation Center for Novel Target and Therapeutic Intervention, Ministry of Education, College of Pharmacy, Chongqing Medical University, Chongqing, China
[2]Key Laboratory of Metabolism and Molecular Medicine, The Ministry of Education, Department of Biochemistry and Molecular Biology, School of Basic Medical Sciences, Fudan University, Shanghai, China
[3]Department of Urology, Zhongshan Hospital, Fudan University, Shanghai, China
[4]College of Basic Medicine, Chongqing Medical University, Chongqing, China
[5]Basic Medicine Research and Innovation Center for Novel Target and Therapeutic Intervention, Ministry of Education, The Second Affiliated Hospital of Chongqing Medical University, Chongqing, China

Acknowledgements The computing work in this paper was partly supported by the Supercomputing Center of Chongqing Medical University. A graphic abstract is created with FigDraw. We would like to express our gratitude to Ms Liu Tao from the Analytical Center of Shimadzu (China) Co., Ltd. for her technical support in mass spectrometry.

Contributors ZW, WJ, LZ, and YD conceived and designed the study, and also interpreted the data. ZW and LZ drafted the manuscript, which WJ and YD subsequently reviewed and edited. JH, LZ, and ZW were responsible for data curation for the resTMe website. QM and JP performed the computational analysis of TCGA bulk RNA data and integrated various batches of scRNA-seq data. ZW defined the TIIMGs and conducted the drug screening on the L1000 platform. ZW also led the computational analysis related to scRNA-seq data, including annotating cell clusters, defining the MPs and their abundance in malignant cells, inferring

MP regulators, and determining the associations between MPs and various drug outcomes. KZ and DW curated the data for validation of the resTMe framework. YD (Fudan University) and SJ collected the clinical information regarding patients treated with anti-PD and gout drugs. ZW, KL, JX, YL, JL, YZ, XW and SW conducted all mouse experiments and performed flow cytometry fluorescence detection. YD is the guarantor. ChatGPT (SciSpace) was used to help revise portions of the manuscript text.

Funding This work was supported by National Key R&D Program of China (2024YFC2815900 to Y.D., 2022YFC2804800 to W.J.); National Natural Science Foundation of China – The Science and Technology Development Fund (NSFC-FDCT Project) (22461160267 to Y.D.); National Natural Science Foundation of China (22137002, to Y.D.); the Major Program of the National Natural Science Foundation of China (22494704 to Y.D., 22494702 to L.Z.); the University Innovation Research Group in Chongqing (CXQT21016 to Y.D.); the Chongqing Talent Program Project (CQYC202003021119 to Y.D.); the High-Level Innovation Platform Cultivation Plan of Chongqing (Y.D.); the Integrated Project of the National Natural Science Foundation of China (92353303 to Y.D.).

Competing interests None declared.

Patient consent for publication Not applicable.

Ethics approval Human tumor samples: The study protocol was approved by the Ethics Committee of Zhongshan Hospital (Shanghai, China; approval no. B2021-198). Patient clinical data was retrospectively collected from the Zhongshan hospital electronic patient record system. Participants gave informed consent to participate in the study before taking part.

Provenance and peer review Not commissioned; externally peer reviewed.

Data availability statement Data are available in a public, open access repository Raw data can be obtained via Genome Sequence Archive in National Genomics Data Center, China National Center for Bioinformation / Beijing Institute of Genomics, Chinese Academy of Sciences (GSA: CRA018225 and CRA018224 for scRNA-seq and bulk RNA-seq respectively) that are publicly accessible at https://ngdc.cncb.ac.cn/gsa. Detailed results of scRNA-Seq data and RNA-Seq were included in Table S5 and Table S7. The website (Responsive TME estimation, resTMe) to identify novel drug combinations with anti-PD therapy is published at http://www.danglab.ac/. The R package resTMe was deposited at https://github.com/DangLab-CQMU/resTMe. All original code has been deposited at https://github.com/DangLab-CQMU/resTMe_code_available and is publicly available as of the date of publication. Any additional information required to reanalyze the data reported in this paper is available from the lead contact upon request.

ORCID iDs
Ziruoyu Wang https://orcid.org/0000-0002-9418-5725
Junchi Hu https://orcid.org/0000-0001-7733-6547
Wei Jiang https://orcid.org/0000-0001-7615-0900
Ling Zhang https://orcid.org/0000-0003-4470-0415
Yongjun Dang https://orcid.org/0000-0001-7237-1132

REFERENCES

1 Kim TK, Vandsemb EN, Herbst RS, *et al*. Adaptive immune resistance at the tumour site: mechanisms and therapeutic opportunities. *Nat Rev Drug Discov* 2022;21:529–40.
2 Gavish A, Tyler M, Greenwald AC, *et al*. Hallmarks of transcriptional intratumour heterogeneity across a thousand tumours. *Nature New Biol* 2023;618:598–606.
3 Chen J, Larsson L, Swarbrick A, *et al*. Spatial landscapes of cancers: insights and opportunities. *Nat Rev Clin Oncol* 2024;21:660–74.
4 Kraehenbuehl L, Weng C-H, Eghbali S, *et al*. Enhancing immunotherapy in cancer by targeting emerging immunomodulatory pathways. *Nat Rev Clin Oncol* 2022;19:37–50.
5 Zhang L, Wang Z, Liu K, *et al*. Targets of tumor microenvironment for potential drug development. *MedComm – Oncology* 2024;3:e68.
6 Limagne E, Nuttin L, Thibaudin M, *et al*. MEK inhibition overcomes chemoimmunotherapy resistance by inducing CXCL10 in cancer cells. *Cancer Cell* 2022;40:136–52.
7 Bernareggi D, Xie Q, Prager BC, *et al*. CHMP2A regulates tumor sensitivity to natural killer cell-mediated cytotoxicity. *Nat Commun* 2022;13:1899.
8 Zeng Q, Saghafinia S, Chryplewicz A, *et al*. Aberrant hyperexpression of the RNA binding protein FMRP in tumors mediates immune evasion. *Science* 2022;378:eabl7207.
9 Schoenfeld AJ, Hellmann MD. Acquired Resistance to Immune Checkpoint Inhibitors. *Cancer Cell* 2020;37:443–55.
10 Lasser SA, Ozbay Kurt FG, Arkhypov I, *et al*. Myeloid-derived suppressor cells in cancer and cancer therapy. *Nat Rev Clin Oncol* 2024;21:147–64.
11 Subramanian A, Narayan R, Corsello SM, *et al*. A Next Generation Connectivity Map: L1000 Platform and the First 1,000,000 Profiles. *Cell* 2017;171:1437–52.
12 Miao Y-R, Zhang Q, Lei Q, *et al*. ImmuCellAI: A Unique Method for Comprehensive T-Cell Subsets Abundance Prediction and its Application in Cancer Immunotherapy. *Adv Sci (Weinh)* 2020;7:1902880.
13 Hao Y, Hao S, Andersen-Nissen E, *et al*. Integrated analysis of multimodal single-cell data. *Cell* 2021;184:3573–87.
14 Stuart T, Butler A, Hoffman P, *et al*. Comprehensive Integration of Single-Cell Data. *Cell* 2019;177:1888–902.
15 Zhang Y, Liu T, Hu X, *et al*. CellCall: integrating paired ligand–receptor and transcription factor activities for cell–cell communication. *Nucleic Acids Res* 2021;49:8520–34.
16 Degasperi A, Amarante TD, Czarnecki J, *et al*. A practical framework and online tool for mutational signature analyses show inter-tissue variation and driver dependencies. *Nat Cancer* 2020;1:249–63.
17 Miao Y-R, Xia M, Luo M, *et al*. ImmuCellAI-mouse: a tool for comprehensive prediction of mouse immune cell abundance and immune microenvironment depiction. *Bioinformatics* 2022;38:785–91.
18 Zhu J, Wang J, Wang X, *et al*. Prediction of drug efficacy from transcriptional profiles with deep learning. *Nat Biotechnol* 2021;39:1444–52.
19 Zou R, Zheng M, Tan M, *et al*. Decreased PTGDS Expression Predicting Poor Survival of Endometrial Cancer by Integrating Weighted Gene Co-Expression Network Analysis and Immunohistochemical Validation. *Cancer Manag Res* 2020;12:5057–75.
20 Schäfer H, Subbarayan K, Massa C, *et al*. Correlation of the tumor escape phenotype with loss of PRELP expression in melanoma. *J Transl Med* 2023;21:643.
21 Shi X, Zhang Y, Wang Y, *et al*. The tRNA Gm18 methyltransferase TARBP1 promotes hepatocellular carcinoma progression via metabolic reprogramming of glutamine. *Cell Death Differ* 2024;31:1219–34.
22 Zhu J, Naulaerts S, Boudhan L, *et al*. Tumour immune rejection triggered by activation of α2-adrenergic receptors. *Nature New Biol* 2023;618:607–15.
23 Bayerl F, Meiser P, Donakonda S, *et al*. Tumor-derived prostaglandin E2 programs cDC1 dysfunction to impair intratumoral orchestration of anti-cancer T cell responses. *Immunity* 2023;56:1341–58.
24 Wang C, Zhang R, He J, *et al*. Ultrasound-responsive low-dose doxorubicin liposomes trigger mitochondrial DNA release and activate cGAS-STING-mediated antitumour immunity. *Nat Commun* 2023;14:3877.
25 Li X, Dong L, Liu J, *et al*. Low-Dose Decitabine Augments the Activation and Anti-Tumor Immune Response of IFN-γ+ CD4+ T Cells Through Enhancing IκBα Degradation and NF-κB Activation. *Front Cell Dev Biol* 2021;9:647713.
26 Yu Q, Dong Y, Wang X, *et al*. Pharmacological induction of MHC-I expression in tumor cells revitalizes T cell antitumor immunity. *JCI Insight* 2024;9:e177788.
27 Zhou L, Liu Y, Wu Y, *et al*. Low-dose radiation therapy mobilizes antitumor immunity: New findings and future perspectives. *Int J Cancer* 2024;154:1143–57.
28 Doshi AS, Cantin S, Prickett LB, *et al*. Systemic nano-delivery of low-dose STING agonist targeted to CD103+ dendritic cells for cancer immunotherapy. *J Control Release* 2022;345:721–33.

29 Nabet BY, Hamidi H, Lee MC, *et al*. Immune heterogeneity in small-cell lung cancer and vulnerability to immune checkpoint blockade. *Cancer Cell* 2024;42:429–43.
30 Hänzelmann S, Castelo R, Guinney J. GSVA: gene set variation analysis for microarray and RNA-seq data. *BMC Bioinformatics* 2013;14:7.
31 Scirgolea C, Sottile R, De Luca M, *et al*. NaCl enhances CD8+ T cell effector functions in cancer immunotherapy. *Nat Immunol* 2024;25:1845–57.
32 Soll D, Chu CF, Sun S, *et al*. Sodium chloride in the tumor microenvironment enhances T cell metabolic fitness and cytotoxicity. *Nat Immunol* 2024.
33 Ribas A, Algazi A, Ascierto PA, *et al*. PD-L1 blockade in combination with inhibition of MAPK oncogenic signaling in patients with advanced melanoma. *Nat Commun* 2020;11:6262.
34 Meng L, Wang Z, Hou Z, *et al*. Study of epirubicin sustained–release chemoablation in tumor suppression and tumor microenvironment remodeling. *Front Immunol* 2022;13:1064047.
35 Pacher P, Nivorozhkin A, Szabó C. Therapeutic Effects of Xanthine Oxidase Inhibitors: Renaissance Half a Century after the Discovery of Allopurinol. *Pharmacol Rev* 2006;58:87–114.
36 Horiuchi H, Ota M, Nishimura S, *et al*. Allopurinol induces renal toxicity by impairing pyrimidine metabolism in mice. *Life Sci (1962)* 2000;66:2051–70.
37 Schlesinger N, Pérez-Ruiz F, Lioté F. Mechanisms and rationale for uricase use in patients with gout. *Nat Rev Rheumatol* 2023;19:640–9.
38 Huang Q, Wu X, Wang Z, *et al*. The primordial differentiation of tumor-specific memory $CD8^+$ T cells as bona fide responders to PD-1/PD-L1 blockade in draining lymph nodes. *Cell* 2022;185:4049–66.
39 Zhang L, Jiang L, Yu L, *et al*. Inhibition of UBA6 by inosine augments tumour immunogenicity and responses. *Nat Commun* 2022;13:5413.
40 Wang T, Gnanaprakasam JNR, Chen X, *et al*. Inosine is an alternative carbon source for CD8+-T-cell function under glucose restriction. *Nat Metab* 2020;2:635–47.
41 Klysz DD, Fowler C, Malipatlolla M, *et al*. Inosine induces stemness features in CAR-T cells and enhances potency. *Cancer Cell* 2024;42:266–82.
42 Mager LF, Burkhard R, Pett N, *et al*. Microbiome-derived inosine modulates response to checkpoint inhibitor immunotherapy. *Science* 2020;369:1481–9.
43 Zilionis R, Engblom C, Pfirschke C, *et al*. Single-Cell Transcriptomics of Human and Mouse Lung Cancers Reveals Conserved Myeloid Populations across Individuals and Species. *Immunity* 2019;50:1317–34.
44 Cheng S, Li Z, Gao R, *et al*. A pan-cancer single-cell transcriptional atlas of tumor infiltrating myeloid cells. *Cell* 2021;184:792–809.
45 Sly LM, McKay DM. Macrophage immunotherapy: overcoming impediments to realize promise. *Trends Immunol* 2022;43:959–68.
46 Tran DH, Kim D, Kesavan R, *et al*. De novo and salvage purine synthesis pathways across tissues and tumors. *Cell* 2024;187:3602–18.
47 Chen T, Chen X, Zhang S, *et al*. The Genome Sequence Archive Family: Toward Explosive Data Growth and Diverse Data Types. *Genomics Proteomics Bioinformatics* 2021;19:578–83.
48 Xue Y, Bao Y, Zhang Z, *et al*. Database Resources of the National Genomics Data Center, China National Center for Bioinformation in 2022. *Nucleic Acids Res* 2022;50:D27–38.